AGU PUBLICATIONS

JGR

Journal of Geophysical Research: Atmospheres

RESEARCH ARTICLE
10.1002/2015JD023108

This article is a companion to *Xu et al.* [2015] doi:10.1002/2015JD023113.

Key Points:
- Synthetic simulation of AERONET multispectral and angular polarimetric data
- Analysis of information content for bimodal size and refractive indices
- Refractive indices errors for each aerosol mode are reduced with polarization

Supporting Information:
- Figures S1–S3 and Table S1

Correspondence to:
J. Wang,
jwang7@unl.edu

Citation:
Xu, X., and J. Wang (2015), Retrieval of aerosol microphysical properties from AERONET photopolarimetric measurements: 1. Information content analysis, *J. Geophys. Res. Atmos.*, *120*, 7059–7078, doi:10.1002/2015JD023108.

Received 13 JAN 2015
Accepted 3 JUN 2015
Accepted article online 4 JUN 2015
Published online 29 JUL 2015

Retrieval of aerosol microphysical properties from AERONET photopolarimetric measurements: 1. Information content analysis

Xiaoguang Xu[1] and Jun Wang[1]

[1]Earth and Atmospheric Sciences, University of Nebraska–Lincoln, Lincoln, Nebraska, USA

Abstract This paper is the first part of a two-part study that aims to retrieve aerosol particle size distribution (PSD) and refractive index from the multispectral and multiangular polarimetric measurements taken by the new-generation Sun photometer as part of the Aerosol Robotic Network (AERONET). It provides theoretical analysis and guidance to the companion study in which we have developed an inversion algorithm for retrieving 22 aerosol microphysical parameters associated with a bimodal PSD function from real AERONET measurements. Our theoretical analysis starts with generating the synthetic measurements at four spectral bands (440, 675, 870, and 1020 nm) with a Unified Linearized Vector Radiative Transfer Model for various types of spherical aerosol particles. Subsequently, the quantitative information content for retrieving aerosol parameters is investigated in four observation scenarios, i.e., I1, I2, P1, and P2. Measurements in the scenario (I1) comprise the solar direct radiances and almucantar radiances that are used in the current AERONET operational inversion algorithm. The other three scenarios include different additional measurements: (I2) the solar principal plane radiances, (P1) the solar principal plane radiances and polarization, and (P2) the solar almucantar polarization. Results indicate that adding polarization measurements can increase the degree of freedom for signal by 2–5 in the scenario P1, while not as much of an increase is found in the scenarios I2 and P2. Correspondingly, smallest retrieval errors are found in the scenario P1: 2.3% (2.9%) for the fine-mode (coarse-mode) aerosol volume concentration, 1.3% (3.5%) for the effective radius, 7.2% (12%) for the effective variance, 0.005 (0.035) for the real-part refractive index, and 0.019 (0.068) for the single-scattering albedo. These errors represent a reduction from their counterparts in scenario I1 of 79% (57%), 76% (49%), 69% (52%), 66% (46%), and 49% (20%), respectively. We further investigated those retrieval errors over a variety of aerosol loading and fine-/coarse-mode prevalence, which indicates that observations in scenario P1 can yield the retrieval of refractive index and single-scattering albedo for both fine and coarse aerosol modes, when aerosol optical depth at 440 nm is larger than 0.2 and 870/1020 nm Ångström exponent ranges between 0.7 and 1.6.

1. Introduction

Atmospheric aerosols play a crucial role in global climate change. They affect Earth's energy budget directly by scattering and absorbing solar and terrestrial radiation and indirectly through altering the cloud formation, lifetime, and radiative properties [*Haywood and Boucher*, 2000; *Ramanathan et al.*, 2001]. However, quantification of these effects in current climate models is fraught with uncertainties. The global average of the aerosol effective radiative forcing was estimated to range from -0.1 to $-1.9\,\mathrm{W\,m^{-2}}$ with the best estimate of $-0.9\,\mathrm{W\,m^{-2}}$ [*Boucher et al.*, 2013], indicating that the cooling effects of aerosol might counteract the warming effects of $1.82 \pm 0.19\,\mathrm{W\,m^{-2}}$ caused by the increase of carbon dioxide since the industrial revolution [*Myhre et al.*, 2013]. The climate effects of aerosol particles depend on their geographical distribution, optical properties, and efficiency as cloud condensation nuclei. Key quantities pertain to the aerosol optical, and cloud-forming properties include particle size distribution (PSD), chemical composition, mixing state, and morphology [*Boucher et al.*, 2013]. While the daily aerosol optical depth (AOD) can be well measured from current satellite and ground-based remote sensing instrumentations [e.g., *Holben et al.*, 1998; *Kaufman et al.*, 2002], the accurate quantification of aerosol radiative effects is in no small part hindered by our limited knowledge about the aerosol PSD and refractive index (describing chemical composition and mixing state). To fully understand the role of aerosol particles in global climate change, further development in observations along with retrieval algorithms for these aerosol microphysical properties from different platforms is thus highly needed [*Mishchenko et al.*, 2004], and the focus of this two-part series study is the characterization of aerosol properties from ground-based passive remote sensing.

There have been continuous efforts in determining aerosol microphysical properties from ground-based measurements of solar radiation since *Ångström* [1929] first suggested an empirical relationship between the spectral dependency of extinction coefficients and the size of aerosol particles. *Curcio* [1961] inferred the aerosol PSD from particulate extinction coefficients in the visible and near-infrared regions. With the effective numerical inversion technique developed by *Phillips* [1962] and *Twomey* [1963], a number of studies soon explored the use of either spectral attenuations or scattered radiances (in a small range of scattering angles) to determine the aerosol PSD [*Twomey and Howell*, 1967; *Yamamoto and Tanaka*, 1969; *Dave*, 1971; *Grassl*, 1971; *Herman et al*., 1971; *King et al*., 1978] or the use of both [*Shaw*, 1979; *Nakajima et al*., 1983; *Kaufman et al*., 1994]. The first operational retrieval algorithm for aerosol microphysical properties was introduced by *Nakajima et al*. [1996], when the automatic scanning spectral radiometer was deployed in the Aerosol Robotic Network (AERONET) [*Holben et al*., 1994, 1998]. All of above mentioned studies treated aerosol particles as homogeneous spheres and with refractive index assumed a priori, though the refractive index can highly impact the optical characteristics, especially the scattering [*Hansen and Travis*, 1974]. *Tanaka et al*. [1982, 1983] developed an inversion library method to estimate the complex refractive index and PSD simultaneously from measurements of polarized sky radiances. Another concept for determining refractive index from solar radiances was developed by *Wendisch and von Hoyningen-Huene* [1994] and *Yamasoe et al*. [1998], which were based on the fact that sensitivities of scattered radiances to the PSD and those to the refractive index are dominated on different scattering angular regions. The current AERONET operational inversion algorithm was developed by *Dubovik and King* [2000], which has heritage from *King et al*. [1978] and *Nakajima et al*. [1983, 1996] but was implemented for simultaneous retrieval of PSD and complex refractive index with sophisticated inclusion of multiple a priori constraints. *Dubovik et al*. [2002, 2006] further implemented the spheroids in the particle shape consideration for desert dust and added fractional volume of nonspherical particles to the inversion products.

AERONET collects not only the multispectral and multiangular radiance observations but also the state of light polarization from various viewing angles over many sites. Unfortunately, the potential value of AERONET polarization measurements in retrieving aerosol microphysical parameters has not been fully exploited. Polarization measurements contain valuable information about aerosol microphysical properties [*Mishchenko and Travis*, 1997; *Cairns et al*., 1997], as the polarization of light is highly sensitive to the aerosol size and refractive index [*Hansen and Travis*, 1974]. Several studies have emphasized the usefulness of the polarimetric observations taken by the ground-based instruments [*Cairns et al*., 1997; *Boesche et al*., 2006; *Emde et al*., 2010; *Zeng et al*., 2008] and airborne sensors [*Waquet et al*., 2009; *Hasekamp and Landgraf*, 2005; *Hasekamp and Landgraf*, 2007; *Dubovik et al*., 2011; *Meland et al*., 2013]. *Vermeulen et al*. [2000] presented a two-step method to retrieve aerosol microphysical properties from polarized radiances: first, the single-scattering albedo and the natural and polarized phase functions were retrieved from transmission and almucantar radiances and polarization in the principal plane and second, the aerosol PSD and refractive index were then derived. With the current AERONET inversion algorithm, *Dubovik et al*. [2006] conducted a case study using polarization data in a UAE^2 (Unified Aerosol Experiment-United Arab Emirates) field campaign [*Reid et al*., 2008]. *Li et al*. [2009] extended the inversion algorithm of *Dubovik et al*. [2006] to include multispectral polarization and demonstrated improved retrievals in the real part of the aerosol refractive index for fine particles and the fraction of spherical particles. However, questions regarding the use of AERONET polarimetric observations for retrieving aerosol microphysical parameters remain unresolved: (1) Practically and quantitatively, what is the magnitude of the information content that exists in AERONET's photopolarimetric measurements for improving the retrieval of aerosol microphysical properties that we now *routinely* obtain from radiance-only measurements? and (2) Hypothetically, how can future upgrades to the AERONET photopolarimetric measurements and inversion algorithm maximize the retrieval information content of AERONET observations? Answering these two questions is relevant not only to the future AERONET instrumentation design but also for the ground-based passive polarimetric remote sensing of aerosols in general.

This is the first paper of a two-part study that aims to conduct more accurate retrievals of aerosol microphysical parameters from AERONET Sun and sky measurements of radiance and polarization. We seek to answer the above questions from a theoretical numerical testbed [*Wang et al*., 2014] by investigating the available information contained in AERONET measurements with and without the

inclusion of polarization data. The purpose of this investigation is to provide the companion paper a theoretical foundation to support actual algorithm development for using polarimetric data for aerosol retrievals [*Xu et al*. 2015]. The testbed used in this paper integrates linearized single-scattering code for spherical particles and linearized vector radiative transfer models, as well as statistical optimization routines. Given the definition of retrieved parameters and observation sets, this testbed can quantify the information content of the observations in terms of the degree of freedom for signal (DFS) and retrieval uncertainty for each retrieved parameter. As presented in *Wang et al*. [2014], the testbed has been used to study the feasibility of combined geostationary satellites to improve retrieval of aerosol properties. To date, however, a systematic evaluation of aerosol information content contained in the ground-based remote sensing system (such as AERONET) has not been carried out and is the focus of this study.

The structure of this paper is as follows. In section 2, we describe the concepts of the inverse problem and information analysis. Then, we introduce the AERONET measurements of radiance and polarization and their forward simulations in section 3. The results of information content and error analysis are presented in section 4. In section 5, we investigate the sensitivity of retrieval uncertainties in aerosol parameters with respect to the aerosol loading and fine/coarse aerosol characteristics. Finally, we summarize in section 6 the general findings of this study and implications for practical algorithm development.

2. Inversion and Information Theory

Let $\mathbf{x}$ denote a state vector that contains n parameters to be retrieved (such as PSD parameters and complex indices of refraction) and $\mathbf{y}$ an observation vector with m elements of measurements (such as multiband radiances from different viewing angles). Furthermore, let $\mathbf{F}$ indicate a forward model (such as the radiative transfer model) that describes the physics of how $\mathbf{y}$ and $\mathbf{x}$ are related. Then, we have

$$\mathbf{y} = \mathbf{F}(\mathbf{x}) + \boldsymbol{\epsilon}, \tag{1}$$

where $\boldsymbol{\epsilon}$ represents experimental errors from both forward modeling and measurement processes.The inverse problem is to solve $\mathbf{x}$ from the measurement $\mathbf{y}$. Provided that errors of measurements and the a priori are characterized by a Gaussian probability distribution function (PDF) and the forward model is linear in the vicinity of the true state, the maximum likelihood solution of the state vector $\hat{\mathbf{x}}$, also called the retrieval or the a posteriori derived with the Bayesian approach, is [*Rodgers*, 2000]

$$\hat{\mathbf{x}} = \mathbf{x}_a + \left(\mathbf{K}^T\mathbf{S}_\epsilon^{-1}\mathbf{K} + \mathbf{S}_a^{-1}\right)^{-1}\mathbf{K}^T\mathbf{S}_\epsilon^{-1}(\mathbf{y} - \mathbf{K}\mathbf{x}_a). \tag{2}$$

Here $\mathbf{S}_a$ is the error covariance matrix of the a priori $\mathbf{x}_a$, representing knowledge of the state before measurement is made. $\mathbf{S}_\epsilon$ is the error covariance matrix of the measurements. $\mathbf{K}$ is the $m \times n$ Jacobian matrix comprising derivatives of each observation with respect to each state parameter or $\partial\mathbf{F}/\partial\mathbf{x}$. The "true state" of state vector is usually nonunique and also follows a Gaussian PDF with the expected value of $\hat{\mathbf{x}}$ and the error covariance matrix $\hat{\mathbf{S}}$ given by

$$\hat{\mathbf{S}}^{-1} = \mathbf{K}^T\mathbf{S}_\epsilon^{-1}\mathbf{K} + \mathbf{S}_a^{-1}. \tag{3}$$

$\hat{\mathbf{S}}$ describes the statistical uncertainties in retrieved $\hat{\mathbf{x}}$ due to measurement noise, forward modeling uncertainty, and a priori error [*Rodgers*, 2000]. The square roots of its diagonals are the 1 sigma uncertainties of each retrieved parameters. With $\hat{\mathbf{S}}$, we can also estimate the uncertainty for any parameter (such as the single-scattering albedo in this study) that can be fully determined by parameters in $\mathbf{x}$ but is not directly retrieved. If such a parameter is a function defined by $\xi = \xi(\mathbf{x})$, then the uncertainty of ξ is [*Rodgers*, 2000]

$$\epsilon_\xi = \sqrt{\sum_{i-1}^{n}\sum_{j=1}^{n}\hat{\mathbf{S}}_{i,j}\frac{\partial\xi}{\partial x_i}\frac{\partial\xi}{\partial x_j}} \tag{4}$$

The Jacobian matrix $\mathbf{K}$ usually serves as a gradient field in the sensitivity analysis and can be a useful indicator of information. For a linear system in the absence of measurement error, the rank of $\mathbf{K}$ indicates independent pieces of information that can be determined from the measurements. In practice, error inevitably presents in

measurements and thus can impact the effective rank. To identify the effective sensitivity of individual measurement to each retrieved parameter, we define the error-normalized (EN) Jacobian matrix by

$$\widetilde{\mathbf{K}} = \mathbf{S}_{\epsilon}^{-\frac{1}{2}}\mathbf{K}\mathbf{S}_{\mathrm{a}}^{\frac{1}{2}}. \tag{5}$$

$\widetilde{\mathbf{K}}$ is also called the "prewhitening" by *Rodgers* [2000]. The superiority of the matrix $\widetilde{\mathbf{K}}$ over the matrix $\mathbf{K}$ is that it compares the observation error ($\mathbf{S}_{\epsilon}^{\frac{1}{2}}$) with the natural variability of the observation vector as expressed by its prior covariance ($\mathbf{K}\mathbf{S}_{\mathrm{a}}^{\frac{1}{2}}$). Any component whose natural variability is smaller than the observation error is not measurable. Therefore, an element $\widetilde{\mathbf{K}}_{i,j}$ less than unity indicates that the measurement component y_i does not contain useful information for determining parameter x_j. In contrast, when $\widetilde{\mathbf{K}}_{i,j} > 1$, the larger the $\widetilde{\mathbf{K}}_{i,j}$ value, the more useful information retained in y_i for determining x_j. Therefore, the $\widetilde{\mathbf{K}}$ matrix provides not only sensitivity of individual measurements to each retrieved parameter but also a capacity metric for those observations to infer retrieved parameters.

The averaging kernel matrix has been widely used to quantify the information gained by making a measurement [e.g., *Rodgers*, 1998; *Hasekamp and Landgraf*, 2005; *Frankenberg et al.*, 2012; *Sanghavi et al.*, 2012]. It is defined by $\mathbf{A} = \partial\hat{\mathbf{x}}/\partial\mathbf{x}$ and thus provides the sensitivity of the retrieval to the true state. Differentiating equation (2) with respect to x, we have

$$\mathbf{A} = \frac{\partial\hat{\mathbf{x}}}{\partial\mathbf{x}} = \left(\mathbf{K}^T\mathbf{S}_{\mathrm{y}}^{-1}\mathbf{K} + \mathbf{S}_{\mathrm{a}}^{-1}\right)^{-1}\mathbf{K}^T\mathbf{S}_{y}^{-1}\mathbf{K} \tag{6}$$

Matrix $\mathbf{A}$ quantifies the ability of the retrieval to infer $\hat{\mathbf{x}}$ given the relationship between $\mathbf{y}$ and $\mathbf{x}$ (i.e., $\mathbf{K}$) and given the observation noise and a priori characterization. Thus, an identity matrix of $\mathbf{A}$ represents a perfect retrieval, while a null matrix of $\mathbf{A}$ indicates that no information can be gained from the observation. The trace of $\mathbf{A}$ is the degree of freedom for signal (DFS), i.e., DFS = Trace($\mathbf{A}$), which represents independent pieces of information that the observation can provide. The diagonal elements of the averaging kernel matrix $\mathbf{A}$, or the *DFS components*, indicate the partial sensitivity of each individual retrieved parameters with respect to their corresponding truth:

$$\mathbf{A}_{i,i} = \frac{\partial\hat{x}_i}{\partial x_i}. \tag{7}$$

Clearly, $\mathbf{A}_{i,i} = \partial\hat{x}_i/\partial x_i = 1$ indicates that the observation is capable of fully characterizing the truth of x_i, while $\mathbf{A}_{i,i} = 0$ indicates that the observation contains zero information on x_i. From the formulation of $\hat{\mathbf{S}}$ and $\mathbf{A}$, we can conclude that only the error covariance and Jacobian matrix, but not the retrieval, are important for the purpose of understanding information content.

Other quantities used for information analysis of a measurement include the Shannon information content (SIC) [*Shannon*, 1948] and the Fisher information matrix. SIC, a widely used quantity [e.g., *Rodgers*, 1998; *Knobelspiesse et al.*, 2012], is defined as the reduction in entropy after the measurement

$$H = \frac{1}{2}\ln|\mathbf{S}_{\mathrm{a}}| - \frac{1}{2}\ln|\hat{\mathbf{S}}| = -\frac{1}{2}\ln|\hat{\mathbf{S}}\mathbf{S}_{\mathrm{a}}^{-1}| = \frac{1}{2}\ln|\mathbf{I}_n - \mathbf{A}|, \tag{8}$$

where $\mathbf{I}_n$ is an identity matrix of order n. Clearly, SIC is highly related to the DFS for the information analysis. In the Gaussian linear case, the Fisher information matrix is equal to the inverse of a posteriori error covariance matrix, $\hat{\mathbf{S}}^{-1}$. The retrieval indeed corresponds to the maximum of a posteriori PDF and the minimum of retrieval error. It is thus straightforward that a higher level of the Fisher information is subject to a smaller retrieval error. Due to their close relationship with the DFS and $\hat{\mathbf{S}}$, we will not present the SIC and Fisher information analysis in this study.

3. Simulation of Measurements

3.1. AERONET Measurements and Definition of Observation Vector

The Cimel Sun photometer equipped at AERONET sites routinely measures direct and diffuse (sky) solar radiances and optionally the light polarization [*Holben et al.*, 1998]. A schematic chart and detail scanning geometry of the Sun photometer are presented in Figure S1 and Table S1 in the supporting information. Direct Sun radiances at various atmospheric window channels from the ultraviolet to near infrared are used to infer the spectral AODs with the Beer-Lambert-Bouguer law [*Smirnov et al.*, 2000]. Sky radiance

Table 1. List of Scenarios of AERONET Observations Used for Information Content Analysis

Scenario	Observations Included[a]	Remark
I1	τ and I_{alm}	Observations used in *Dubovik and King* [2000] algorithm
I2	τ, I_{alm}, and I_{pp}	Scenario I1 plus principal plane radiances
P1	τ, I_{alm}, I_{pp}, and $DOLP_{pp}$	Scenario I2 plus principal plane polarization
P2	τ, I_{alm}, and $DOLP_{alm}$	Scenario I1 plus almucantar polarization

[a]Variables are for four spectral wavelengths, i.e., 440, 675, 870, and 1020 nm.

measurements, which are performed at 440, 670, 870, and 1020 nm bands with full width spectrum at half maximum of 10 nm, are acquired from both solar almucantar and solar principal plane. An almucantar is a series of measurements taken at the viewing angle of the Sun for 76 specified relative azimuthal angles (Table S1). To achieve a wide enough range of scattering angles, almucantar scans are usually made at an optical air mass of 1.7 or more (corresponding to solar zenith angle larger than ~50°). The principal plane sequence for each spectrum performs right after almucantar scans. It begins with a Sun observation, moves 6° below the sunray, sweeps up through the Sun, and ends at a scattering angle of 150° or viewing angle achieves horizon, collecting radiances from up to 42 viewing angles (Table S1). Hereinafter, we will use I_{alm} and I_{ppl} to represent the sky radiances from the solar almucantar and solar principal plane, respectively.

Light polarization measurements are performed with three polarizers placed 60° between each axial direction. The total radiance can be derived by

$$I_{pp} = \frac{2}{3}(I_1 + I_2 + I_3), \tag{9}$$

where I_1, I_2, and I_3 are radiance measured with these three polarizers, respectively. The degree of linear polarization (DOLP) of skylight is inferred by

$$DOLP_{pp} = \frac{2\left(I_1^2 + I_2^2 + I_3^2 - I_1 I_2 - I_2 I_3 - I_3 I_1\right)^{1/2}}{I_1 + I_2 + I_3}. \tag{10}$$

It should be noted that we prefer to use $DOLP_{pp}$ instead of polarized radiance in our inversion, since as a relative quantity $DOLP_{pp}$ is more accurate. Polarization measurements are made every hour (right after principal plane scans) at 870 nm in the principal plane at 5° increments between viewing zenith angle of −85° and +85° (as shown in Figure S1 and Table S1). Polarization measurements are optional depending on the instrument version and configuration. They are currently available mostly over European and African stations. Recently, multispectral polarizations have also been taken with a newer-generation Cimel Sun photometer (CE318-DP) at some sites [*Li et al.*, 2009] and the UAE^2 fields campaign [*Reid et al.*, 2008]. Here we focus our study on using multispectral polarizations for the inversion of aerosol parameters.

In order to investigate the merit of synergizing various observations in the inversion, we define four different scenarios of observation vectors, i.e., I1, I2, P1, and P2, as summarized in Table 1. The observation vector in scenario I1 comprises direct Sun AODs and solar almucantar radiances (I_{alm}) at 440, 675, 870, and 1020 nm. Scenario I2 includes measurements in scenario A and the total radiances (I_{PP}) at the same four wavelengths observed in the solar principal plane. Observations in scenario P1 are defined to further include $DOLP_{PP}$ at those four wavelengths. Lastly, scenario P2 observations comprise basic measurements in scenario I1 plus almucantar polarization ($DOLP_{alm}$) at the same wavelengths. The $DOLP_{alm}$ is not routinely measured by any current Sun photometer, but we include it for a comparative analysis. Measurements defined in scenario I1 represent observations used by the current AERONET operational inversion and thus serve as a control experiment. From scenario I2, we can investigate the synergy of radiances in both the solar almucantar and solar principal plane. Scans in the solar principal plane can achieve larger scattering angles and thus may contain additional scattering information. And with scenarios P1 and P2 we will be able to evaluate the potential of adding polarization in the inversion. In addition, we simulate each scenario under various solar zenith angles from 40° to 75° (with 5° increments) to cover different times of a day.

We exclude I_{ppl} in our analysis because sky radiance in the solar principal plane can also be obtained during the polarization scan (I_{pp}). I_{ppl} and I_{pp} are different in the viewing angle sequences, but they generally share a similar range of scattering angles. Thus, one is redundant with the other. We also exclude analysis of

Table 2. The Aerosol Parameters Defined for Both Fine and Coarse Aerosol Modes[a]

Mode	r_{eff} (μm)	v_{eff}	$\mathbf{m_r}$	$\mathbf{m_i}$	ω_A
Fine	0.21 (80%)	0.25 (80%)	1.44, 1.44, 1.43, 1.42 (0.15)	0.009, 0.011, 0.012, 0.011 (0.01)	0.95, 0.93, 0.92, 0.91 (0.151)
Coarse	1.90 (80%)	0.41 (80%)	1.56, 1.55, 1.54, 1.54 (0.15)	0.004, 0.003, 0.003, 0.002 (0.005)	0.84, 0.91, 0.93, 0.96 (0.198)

[a]The complex refractive index $m_r - m_i i$ and single-scattering albedo ω_A are reported at 440, 675, 870, and 1020 nm. Bracketed values are assumed a priori error in relative for r_{eff} and v_{eff} and in absolute for m_r, m_i, and ω_A.

monochromatic polarization (at 870 nm), currently measured on many AERONET sites, because single-band polarization measurements contain much less information than multiband ones and newer-generation Sun photometers with multiband polarization capacity will be deployed at more AERONET sites. The specific viewing geometrical angles used in our calculation are shown in bold in Table S1.

3.2. Definition of the State Vector

The state vector **x** contains 11 pairs (a total number of 22) of parameters characterizing aerosol properties in the fine and the coarse modes, respectively: the columnar volume concentration V_0, the effective radius r_{eff}, the effective variance v_{eff}, and the complex refractive index ($m_r - m_i i$) at 440, 675, 870, and 1020 nm. r_{eff} and v_{eff} are two commonly used size parameters in the aerosol radiative quantification, because different types of size distribution function having the same values of r_{eff} and v_{eff} possess similar scattering and absorption properties [*Hansen and Travis*, 1974]. In line with many studies [*Schuster et al*., 2006; *Hasekamp and Landgraf*, 2005, 2007; *Mishchenko et al*., 2007; *Waquet et al*., 2009], we assume that aerosol particles are spherical particles following a bimodal lognormal PSD function:

$$\frac{dV}{d\ln r} = \sum_{i=1}^{2} \frac{V_0^i}{\sqrt{2\pi}\ln\sigma_g^i} \exp\left[-\frac{\left(\ln r - \ln r_v^i\right)^2}{2\ln^2\sigma_g^i}\right] \tag{11}$$

where r_v and σ_g are the volume geometric median radius and the geometric standard deviation, respectively. The superscript *i* indicates size mode and later is replaced by "f" and "c" to represent a fine mode and a coarse mode, respectively. An advantage of the lognormal distribution is that the standard deviation is identical for the number, area, and volume PSDs, and therefore, the median radius for the number and area PSDs can be derived from the volume median radius r_v [*Hansen and Travis*, 1974]. Furthermore, r_{eff} and v_{eff} can also be converted to or from those geometric parameters. We assume in this study the size range for fine-mode particles from 0.01 to 10 μm and for the coarse-mode particles from 0.05 to 20 μm, both covering $> 99.9\%$ of idealistic aerosol particle size range of (0, +∞).

Table 2 displays size parameters, refractive indices, and single-scattering albedo (ω_A) for each size mode adopted for error and information analysis. The r_{eff} and v_{eff} of fine-mode particles are chosen to represent sulfate aerosols at relative humidity of 60% [*Drury et al*., 2010]. The refractive indices of fine-mode particles correspond to water-soluble aerosols obtained from OPAC database [*Hess et al*., 1998], while the coarse mode is for large spherical particles with refractive index from *Patterson et al*. [1977] and *Wagner et al*. [2012]. We found that these selected aerosol parameters are in good agreement with the climatological aerosol properties obtained in the companion paper [*Xu et al*., 2015].

In order to include various atmospheric conditions, we simulate three types of aerosols—each with different relative percentage between the coarse and fine modes—(I) fine particles dominated, (II) well mixed, and (III) coarse particles dominated. As listed in Table 3 and illustrated in Figure 1, fine-mode fractions in terms of

Table 3. The Aerosol Scenarios Adopted for Numerical Experiments[a]

Aerosol Type	V ($\mu m^3 \mu m^{-2}$)	fmf_V	τ	τ_1/τ	AE	ω_A
I. Fine dominated	0.149	0.8	1.0, 0.58, 0.36, 0.25	0.97, 0.95, 0.92, 0.88	1.5	0.95, 0.93, 0.92, 0.91
II. Well mixed	0.220	0.5	1.0, 0.61, 0.41, 0.32	0.90, 0.83, 0.74, 0.65	1.3	0.94, 0.93, 0.92, 0.93
III. Coarse dominated	0.425	0.2	1.0, 0.71, 0.57, 0.50	0.69, 0.55, 0.42, 0.32	0.82	0.91, 0.92, 0.92, 0.94

[a]Values for τ and ω_A are listed respectively for spectral wavelength of 440, 675, 870, and 1020 nm. The AE is reported between 440 and 870 nm.

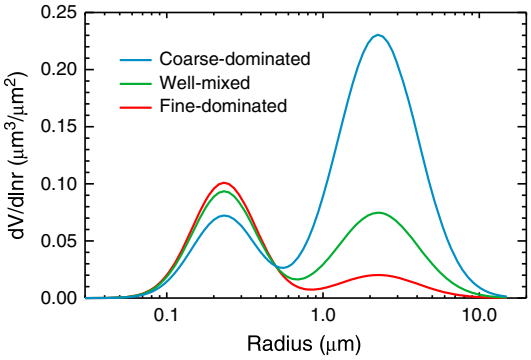

Figure 1. Volume size distribution for the aerosol types adopted for the information analysis. Relevant aerosol parameters are summarized in the Tables 2 and 3.

volume (fmf_v) are defined as 0.8, 0.5, and 0.2 for these three types, respectively. Aerosol volumes are scaled as necessary to maintain a normalized AOD at 440 nm corresponding to a moderate hazy condition ($\tau_{440} = 1.0$). The spectral aerosol optical depths τ, single-scattering albedo ω_A, and the Ångström exponent (AE) are calculated and also shown in Table 3.

3.3. Forward Model

The AERONET observations were simulated by a numerical testbed that was specifically developed for analysis and inversion of remote sensing observations [*Wang et al.*, 2014]. The testbed consists of seven modules for forward calculations of synthetic observations and a module for optimal inversion. The forward modeling includes a linearized vector radiative transfer model (VLIDORT), a linearized Mie code, a linearized T-Matrix code, and modules calculating Rayleigh scattering and gas absorption, plus a surface model computing various bidirectional reflectance/polarization distribution functions (BRDF/BPDF). Such forward modeling framework thus constitutes a Unified Linearized Vector Radiative Transfer Model, or UNL-VRTM. Required inputs for UNL-VRTM are atmospheric profiles (of pressure, temperature, and gaseous mixing ratio), aerosol vertical profiles, aerosol microphysical parameters (size distribution and complex refractive index), and surface characterization parameters. Users are allowed to specify up to two aerosol size modes. Each individual mode is associated with its own loading, vertical profile, particle size distribution, and complex refractive index.

The VLIDORT model [*Spurr*, 2008] integrated in the UNL-VRTM allows the simulation of the full vector of Stokes parameters:

$$\mathbf{I} = [I, Q, U, V]^{\mathrm{T}}. \tag{12}$$

The degree of linear polarization (DOLP) then can be computed to be consistent with the AERONET measurements defined in the equation (10):

$$\mathrm{DOLP} = \frac{\left(Q^2 + U^2\right)^{\frac{1}{2}}}{I}. \tag{13}$$

Along with simulating synthetic observations, i.e., multiband skylight radiances and DOLP reached to the surface level in both solar almucantar and solar principal planes, the UNL-VRTM also analytically computes weighting functions (or Jacobian matrix **K**) of those synthetic data with respect to parameters in the state vector. The Jacobian matrix and error characterization of measurements and a priori constraints are supplied to an optimal estimation procedure for information content analysis. The design of the testbed aims to create a flexible framework to allow simulation and inversion of observations from various platforms. It can be applied to ground-based observations (such as those from the AERONET) and satellite observations. For example, we have explored the aerosol information content of observations from the future Tropospheric Emissions: Monitoring of Pollution and Geostationary Coastal and Air Pollution Events missions [*Wang et al.*, 2014].

While not as important as that for estimating the upwelling shortwave radiances, accurately characterizing the surface reflectance and depolarization can minimize the possible error in the simulation of downwelling radiation. For total reflectance, we parameterize the surface BRDF using the reciprocal-Ross-Li kernels [*Wanner et al.*, 1995], which are applied in Moderate Resolution Imaging Spectroradiometer (MODIS) surface retrieval products [*Lucht et al.*, 2000]. These three kernels represent scatterings respectively from a Lambertian surface, a surface within a dense vegetation canopy, and a surface with larger gaps between objects accounting for self-shadowing. Amplitude factors for these kernels at AERONET bands are chosen from MODIS products at Beijing during February 2011 to represent a typical urban site. We also use a BPDF model introduced by *Maignan et al.* [2009] for the angular polarized

radiance, which was based on the Fresnel coefficients of light reflectance from the surface and fitted to a satellite senor called Polarization and Directionality of Earth's Reflectances.

3.4. Errors of Observations and A Priori

As discussed in section 2, the resulting DFS and retrieval error depend on the error specifications for the state of a priori and for the observations. A realistic uncertainty characterization is thus of crucial importance. We consider the measurement errors consisting of uncertainties that take place in both of the observation process and the forward modeling. The uncertainties of AOD and radiance measurements taken by a well-calibrated Cimel Sun photoemter usually do not exceed 0.01–0.02 and 3–5%, respectively [*Holben et al*., 1998, 2006; *Li et al*., 2008]. For polarization measurements calibrated with the approach of *Li et al*. [2010], the uncertainty of DOLP was estimated to be 0.005 for the newer-generation CE318-DP Sun photometer and 0.01 for the older CE318 generation. In thus study, we conservatively choose absolute error of 0.02 for AOD and relative uncertainty of 5% for I_{alm} and I_{pp}, which are the same as *Dubovik et al*. [2000]. We set the absolute uncertainty of DOLP as 0.01 in consistent with *Li et al*. [2009] and *Waquet et al*. [2009]. We consider the forward modeling error incurred by the limited knowledge of surface reflectivity; the amplitude factor for each BRDF kernel is assumed to have 20% relative uncertainty. However, we ignore the error in the BPDF because the polarized reflectance of the land surface is usually spectrally invariant and tends to be smaller than 0.02–0.04 [*Nadal and Breon*, 1999; *Maignan et al*., 2009].

As a result, the observation error covariance matrix is defined by

$$\mathbf{S}_{\epsilon} = \mathbf{S}_{y} + \mathbf{K}_{b}\mathbf{S}_{b}\mathbf{K}_{b}^{T}, \tag{14}$$

where $\mathbf{S}_y$ is the error covariance matrix representing the uncertainty occurring in the measuring process, $\mathbf{S}_b$ is the error covariance matrix for spectral BRDF amplitude factors ($\mathbf{b}$), and $\mathbf{K}_b$ is the Jacobian matrix of measurements $\mathbf{y}$ with respect to $\mathbf{b}$. Similar to *Dubovik et al*. [2000], we use zero off-diagonal elements for $\mathbf{S}_y$ by assuming that errors are independent between measurements. Errors for $\mathbf{b}$ are also assumed to be noncorrelated, which gives a diagonal matrix of $\mathbf{S}_b$

As discussed in *Dubovik et al*. [2000], the surface characteristics appear to have much less effect in AEROENT retrieval than in satellite retrievals, because AERONET measures downward sky radiances. According to our simulation, the relative error in radiances incurred by surface BRDF uncertainties is 0.7% by averaging all Sun photometer observation geometries, with the maximum of about 2% occurring at the near-horizontal viewing angles. The contribution of the term $\mathbf{K}_b\mathbf{S}_b\mathbf{K}_b^T$ to $\mathbf{S}_{\epsilon}$ in equation (14) is then less than 2% (the square of 0.7% to the square of 5%).

The uncertainties associated with the a priori knowledge are given in Table 2. We consider that the aerosol columnar volume concentrations for both modes are unknown with a relative uncertainty of 100%. Uncertainties for aerosol microphysical parameters are based on aerosol climatology of the companion paper and are consistent with *Dubovik et al*. [2002] and *Waquet et al*. [2009]. As listed in Table 2, the relative error of r_{eff} and v_{eff} are 80% for both aerosol modes, and the absolute error is assumed to be 0.15 for m_r of both modes, 0.01 for fine-mode m_i, and 0.05 for coarse-mode m_i. These prescribed a priori uncertainties give an error of 0.15 and 0.20 for aerosol single-scattering albedo (ω_A) of the fine mode and the coarse mode, respectively. We also assume that the a priori uncertainties are independent between retrieved parameters by using zero off-diagonal elements for $\mathbf{S}_a$.

4. Results

Following the approach stated in section 3, we have simulated the AERONET photopolarimetric measurements for those three defined aerosol types. The simulated radiances (I_{alm}) on the solar almucantar plane and the degree of linear polarization ($DOLP_{pp}$) on the solar principal plane are illustrated in Figure 2 for aerosols of the well-mixed type (Table 3) with solar zenith angle of 55°. These simulations for other aerosol types (as shown in Figure S2 in the supporting information) and other solar zenith angles are of similar pattern. According to Figure 2a, I_{alm} decreases as the scattering angle increases, resulting from forward-dominated scattering phase function of aerosol particles. The maximum $DOLP_{PP}$ takes place at the scattering angle of 90° as a result of composite effect of Rayleigh and aerosol scattering, while the smaller $DOLP_{PP}$ values dominate at the small scattering angles because of the predominance of diffracted light (Figure 2b). With

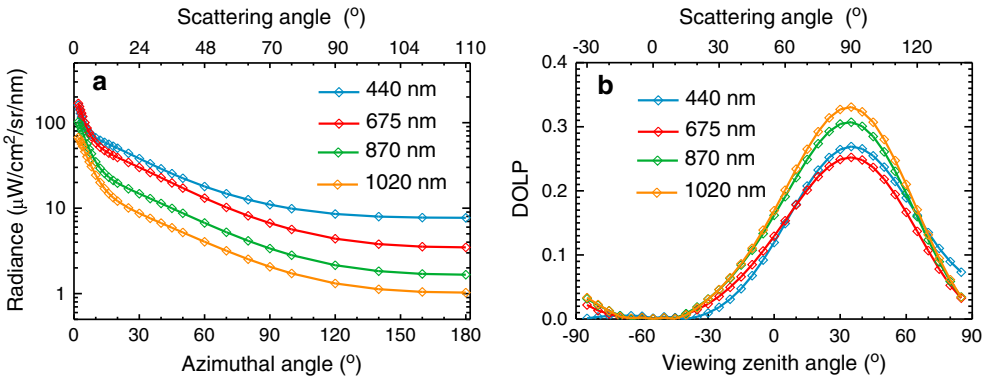

Figure 2. (a) Simulated radiances in the solar almucantar plane as a function of azimuth angle. (b) Simulated degree of linear polarization (DOLP) in the solar principal plane as a function of view zenith angle. Simulations are for the well-mixed aerosol type with columnar AOD of 1.0 at 440 nm as shown in Table 3. Solar zenith angle is 55°, and top abscissas show corresponding scattering angles.

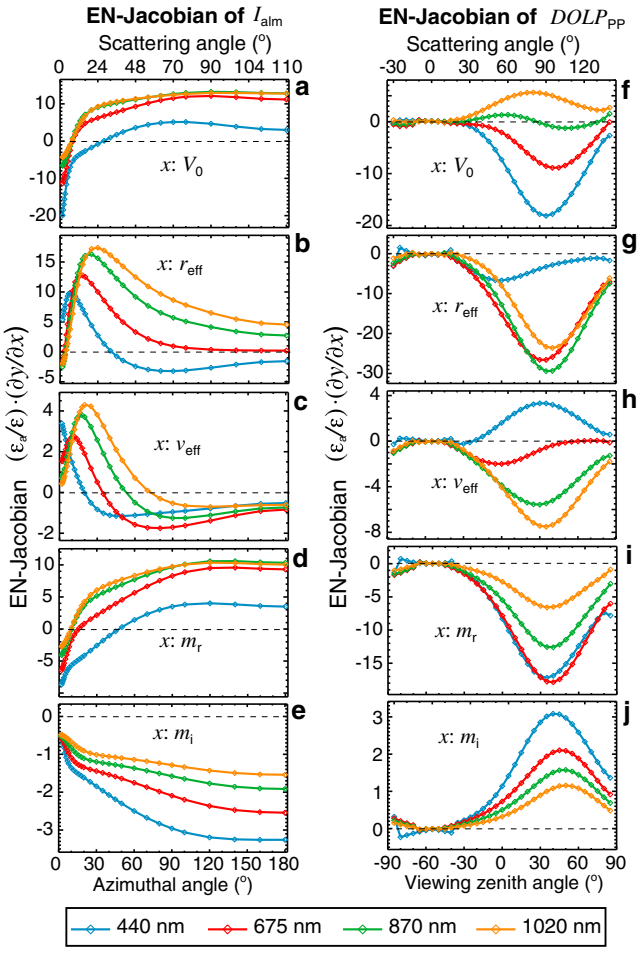

Figure 3. Error-normalized Jacobians of (a–e) almucantar radiances I_{alm} and (f–j) degree of linear polarization $DOLP_{PP}$ with respect to retrieved aerosol parameters in the *fine* mode: V_0 (Figures 3a and 3f), r_{eff} (Figures 3b and 3g), v_{eff} (Figures 3c and 3h), m_r (Figures 3d and 3i), and m_i (Figures 3e and 3j). Simulations use well-mixed aerosols of type II with columnar AOD of 1.0 at 440 nm and solar zenith angle of 55°. The top and bottom abscissas are respectively the scattering angle and Sun photometer scanning geometries.

the synthetic data and relevant error characterizations, we have computed the error-normalized (EN) Jacobian matrix, DFS, and a posteriori error to evaluate the capacity of AERONET measurements in inferring aerosol microphysical properties. Our analysis mainly focuses on the comparison of those quantities between measurements with and without including polarization so that we can understand the importance of adding polarization for the retrieval.

4.1. EN Jacobian Matrix $\widetilde{\mathbf{K}}$

We compare the EN Jacobians for the I_{alm} and $DOLP_{PP}$ in both Figures 3 and 4 to explore the importance of $DOLP_{PP}$ measurements to the retrieval. Distinct patterns of EN Jacobians can be found between the $DOLP_{PP}$ and I_{alm} over the scattering angle. As shown in Figures 3a and 4a, the radiance at scattering angles less than ~10° decreases with increasing fine-mode aerosol loading (e.g., negative $\partial I_{alm}/\partial V_0$) and increases with increasing coarse-mode aerosol loading (e.g., positive $\partial I_{alm}/\partial V_0$), whereas the sensitivity of the I_{alm} to V_0 at larger scattering angles is more positive in the fine mode and less positive in the coarse mode. This occurs because large particles scatter more radiation than small particles at near-forward scattering angles [*van de Hulst*, 1981]. In contrast, the $DOLP_{PP}$ presents profound sensitivity to the V_0

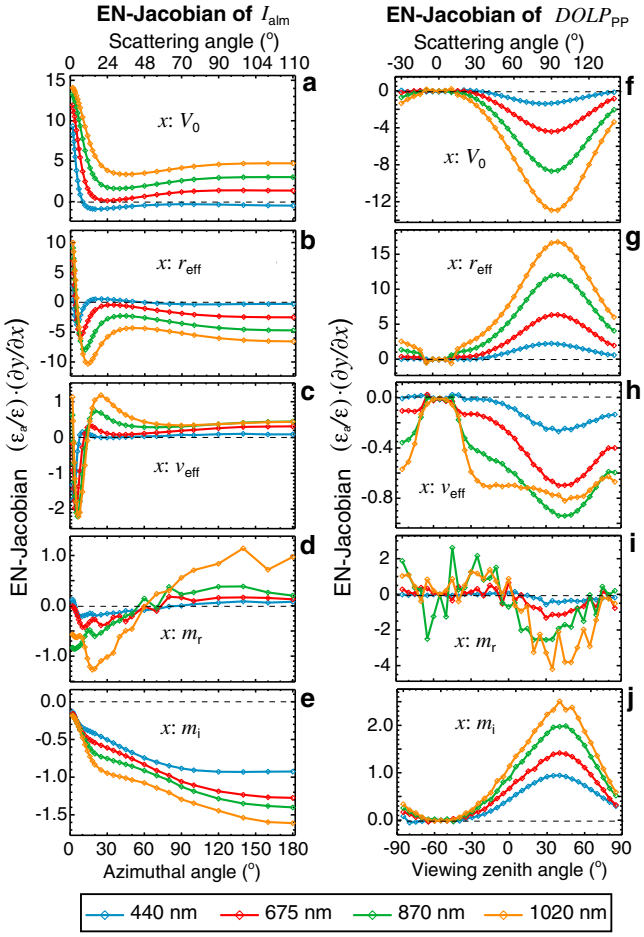

Figure 4. Same as Figure 3 but for parameters of aerosol in the *coarse* mode.

of aerosol in both modes at the scattering angles between 45° and 135° (Figures 3f and 4f).

Furthermore, I_{alm} and $DOLP_{PP}$ also have complementary aerosol information as shown by the variations of their Jacobians on the spectral wavelength. For example, the EN Jacobians for I_{alm} with respect to the fine-mode V_0 express lowest at 440 nm (blue curve in Figure 3a), but those for $DOLP_{PP}$ at 440 nm (blue curve in Figure 3f) are largest ones among these four spectral bands. Indeed, variations of these sensitivities with wavelength are mainly determined by the change of size parameter η, which is defined as the ratio of the particle size to the applied spectral wavelength, $\eta = 2\pi r_{eff}/\lambda$. The $DOLP_{PP}$ in scattering angles near 90° approaches unity under pure Rayleigh scattering regime where $\eta << 1$. When the η increases, the value of $\partial DOLP_{PP}/\partial V_0$ decreases and transits into negative at $\eta \sim 2$, reaches negative maxima at $\eta \sim 10$, then increases and slowly transits back to positive when η is as large as ~40 [*Hansen and Travis*, 1974]. The magnitude of the η at these four bands ranges from 3.0 to 1.3 for the fine-mode particles and from 27 to 11 for the coarse-mode particles. Therefore, we can understand that (i) the sensitivity of $DOLP_{PP}$ to the fine-mode V_0 is positive at 1020 nm due to the small size parameter $\eta = 1.3$ (orange curve in Figure 3f); (ii) this sensitivity gets weaker at 675 nm to 870 nm and transits to negative at 440 nm as η increases (Figure 3f); and (iii) this sensitivity for aerosol in the coarse mode is more negative for longer wavelengths that are corresponding to smaller values of η.

We also note that sensitivity of the I_{alm} to PSD parameters dominates for scattering angles less than ~40° (Figures 3b, 3c, 4b, and 4c), while its sensitivity to m_r and m_i prevails at larger scattering angles (Figures 3d, 3e, 4d, and 4e). In the near-forward scattering angular regions, the dominant scattering effect is the diffraction of light, which essentially depends on the size of particles and is independent of the index of refraction [*van de Hulst*, 1981; *Hansen and Travis*, 1974]. The $DOLP_{pp}$, in contrast, is sensitive to both the aerosol size and the refractive index at scattering angles from 45° to 135° (Figures 3f–3j and 4f–4j). Variations of the sensitivity among spectral bands can be explained by the wavelength-dependent size parameters as discussed in the above paragraph.

Overall, the $DOLP_{PP}$ EN Jacobians have similar or larger magnitudes to these of I_{alm}, indicating that the $DOLP_{pp}$ measurements possess equal or larger information for the inversion of these aerosol properties. Adding such complementary $DOLP_{PP}$ measurements to the current radiance-only inversion can potentially increase the retrieval accuracy. The magnitude of EN Jacobian elements varies among retrieved parameters, which leads to the variability of retrieval accuracy. The EN Jacobians with respect to the V_0 and r_{eff} of both modes and the fine-mode v_{eff} and refractive index are larger than those of other parameters. Correspondingly, these parameters are expected to achieve higher accuracy in the retrieval. While the maxima in EN Jacobians of I_{alm} with respect to the coarse-mode refractive index at 870 and

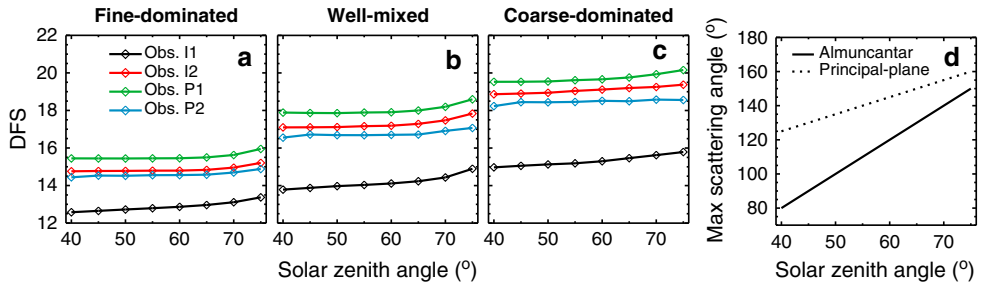

Figure 5. Degree of freedom for signal (DFS) as a function of solar zenith angle for retrieving all 22 parameters when using aerosol type of (a) fine dominated, (b) well mixed, and (c) coarse dominated. Four differently colored curves denote four observation scenarios defined in Table 1. (d) Maximum scattering angles that can be reached by the almucantar and the principal plane scans.

1020 nm slightly exceed unity (Figures 4d and 4e), larger counterparts for $DOLP_{PP}$ (Figures 4i and 4j) will likely result in improved retrievals. In contrast, magnitudes of EN Jacobian for both I_{alm} and $DOLP_{PP}$ with respect to coarse-mode refractive index at 440 and 675 nm are smaller than unity across the whole angular range. Adding polarization may not improve the retrieval for coarse-mode refractive index at those shorter wavelengths in such aerosol scenario. However, the consideration of spectral dependence of refractive index by using the smoothness constraints will potentially resolve this problem [*Dubovik*, 2004; *Xu et al*., 2015].

4.2. Information Content and Retrieval Error

We calculated the averaging kernel matrix **A**, DFS, and a posteriori error for retrieved parameters from these four scenarios of observation defined in Table 1. Figures 5a–5c illustrate how the DFS varies with the solar zenith angles for three defined aerosol types. The DFS in the scenario I2 (red curves) ranges from

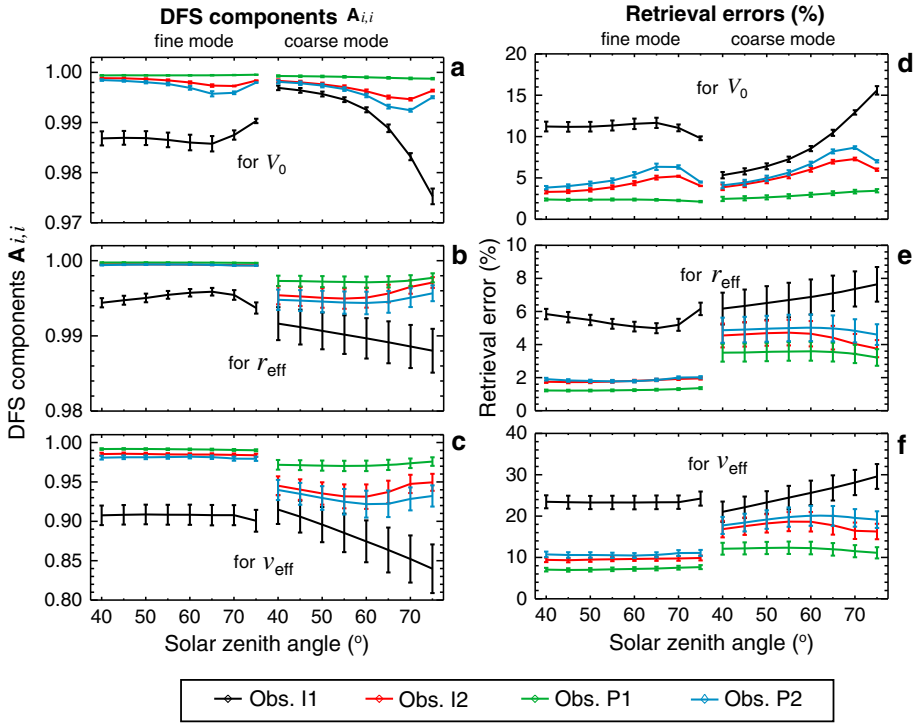

Figure 6. (a–c) DFS components and (d–f) retrieval uncertainty as a function solar zenith angles with different observation scenarios defined in Table 1. Quantities are averages for three aerosol types defined in Table 3, and error bars represent one fifth of standard deviation. Three rows from top to bottom are respectively for retrieving V_0, r_{eff}, and v_{eff}. In each panel, shown in the left is for the fine mode and in the right is for the coarse mode.

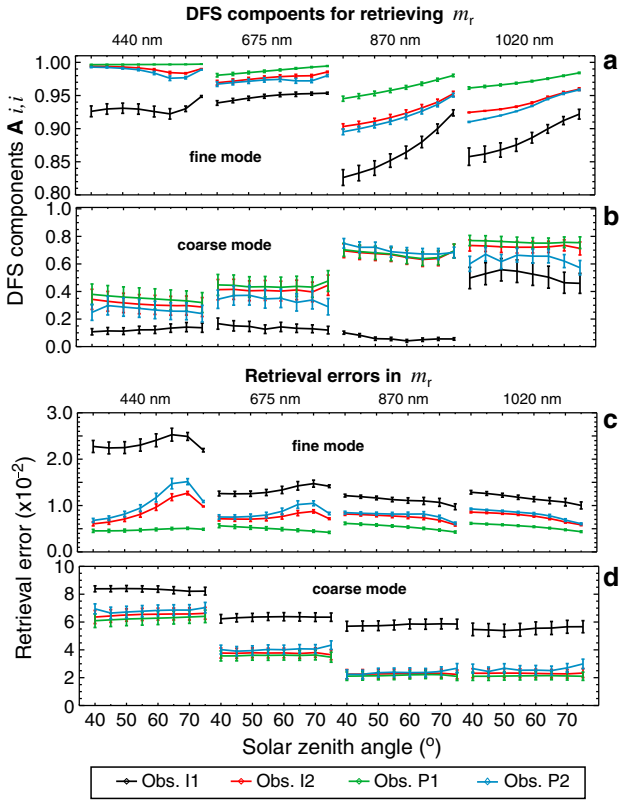

Figure 7. Same as Figure 6 but for (a and b) DFS components and (c and d) retrieval uncertainty for retrieving real-part refractive index m_r in four wavelength bands. Figures 7a and 7c are for the fine aerosol mode, while Figures 7b and 7d are for the coarse mode.

14 to 15 for the fine-dominated aerosol model, and from 17 to 19 for other two aerosol models, about 2–3 higher than those using AODs and I_{alm} measurements in the scenario I1 (black curves), indicating that sky radiances in the principal plane (I_{PP}) contain additional information. The scenario P1 (green curves), which comprises solar almucantar sky radiances and principal plane polarimetric radiances at four wavelengths, further increases DFS by 1–2. Observations in the scenario P2 (blue curves)—radiance and polarization in the almucantar plane—yield DFS values slightly below those in the scenarios I2 and P1. Therefore, from Figure 5 we conclude that adding measurements in the solar principal plane into the inversion significantly increases the information content for aerosol properties, especially when combining the I_{PP} and $DOLP_{PP}$. We also note that the DFS increases with solar zenith angle for all cases. Observations in larger solar zenith angle enable a wider range of scattering angles (Figure 5d) and thus contain more information on the aerosol scattering phase function and in turn on the aerosol microphysical parameters.

We illustrate the DFS components $A_{i,i}$ in Figure 6 for the V_0, r_{eff}, and v_{eff} and in Figures 7 and 8 for the m_r and m_i, respectively. Also shown in those figures are the a posteriori errors, which are the diagonal elements of $\hat{\mathbf{S}}^{\frac{1}{2}}$. It should be noted that errors for V_0, r_{eff}, and v_{eff} are in terms of relative uncertainties (%), while errors in the m_r and m_i are absolute quantities. Curves of four different colors in each panel indicate these defined four observation scenarios and are averages for the three aerosol types. Error bars represent *one fifth* of the standard deviations among the three aerosol types (the use of the *one-fifth* scale is only for plotting purpose). These error bars thus depict the variability of the DFS component and retrieval error over the fine-mode fraction (fmf_v). Mean retrieval uncertainties averaged over various solar zenith angles are summarized in Table 4. We discuss these results for each retrieved parameter in detail as following.

4.2.1. Aerosol PSD

Among the 22 elements in the state vector, the V_0, r_{eff}, and v_{eff} describe the aerosol PSD. According to Figures 6a–6c, observations in the scenario P1 (green curves) always yield the highest DFS components for inferring PSD parameters in both the fine and coarse modes, followed by observations from the scenarios I2 (red) and P2 (blue) and lastly the scenario I1 (black). As a consequence, the a posterior errors are found smallest for the scenario P1 and largest for the scenario I1 (Figures 6d and 6e). Retrieval errors in the scenario I1 (black curves) are 5–15% for V_0, 5–9% for r_{eff}, and 20–30% for v_{eff} which vary with solar zenith angles. In contrast, retrieval errors in the scenario P1 (green curves) are reduced to ~2.5% (3%), 1% (3.5%), and 7% (20%) for the fine (coarse) mode. From observations in the scenarios P2 and I2, one can retrieve V_0, r_{eff}, and v_{eff} of errors lying between the scenarios I1 and P1, though slightly larger in the scenario P2. In addition, higher DFS components and smaller retrieval errors are found for the fine-mode parameters than those for the coarse mode, because radiances and polarization are, in particular, more sensitive to aerosol parameters in the fine mode as shown in the contrast between Figures 3 and 4.

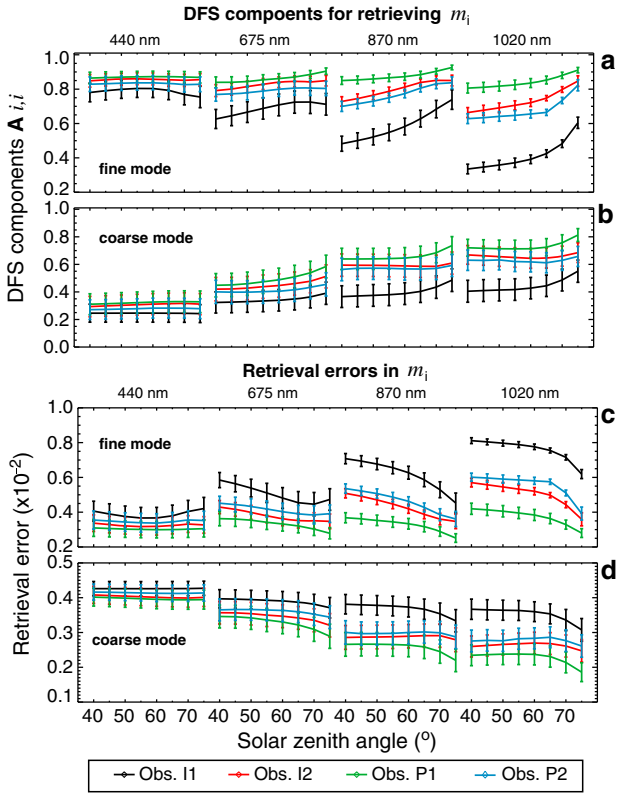

Figure 8. Same as Figure 7 but for retrieving imaginary part refractive index m_i.

We also note that in the scenario I1, DFS components for the coarse-mode parameters decrease with increasing solar zenith angle, while no obvious trend can be found for the fine-mode parameters. This can be explained by the low sensitivity of the I_{alm} to the coarse-mode V_0, r_{eff}, and v_{eff} at large scattering angles as shown in Figures 4a–4c. Higher sensitivities occur at scattering angles below ~30°; the increase in SZA results in a smaller number of measurements in the near-forward scattering angular regions and thus leads to larger retrieval errors. However, these trends turn to be weaker or negligible in other observation scenarios, especially the scenario P1. We can understand this from two aspects. First, observations from principal plane can add additional measurements near the forward scattering region. Second and most importantly, the added polarization measurements in the scenarios P1 and P2 contain additional information that is independent of the scattering angle limitation as discussed in section 4.1.

Overall, the increase in DFS components by adding polarization measurements is less than 0.1 for retrieving V_0, r_{eff}, and v_{eff}, because radiances alone contain abundant information. The retrieval accuracy in aerosol PSD from observations of all scenarios exceeds the requirements for better quantifying aerosol climate radiative forcing identified by *Mishchenko et al.* [2004]. Even so, the addition of multiband $DOLP_{PP}$ measurements to the inversion can still yield up to ~70% retrieval error reduction in the fine-mode and up to ~50% reduction in the coarse-mode aerosol PSD parameters.

4.2.2. Refractive Indices

As shown in Figures 7a and 7b, different magnitudes prevail in the DFS components for the m_r between fine and coarse modes and among different observation scenarios. For example, DFS components for aerosols in the fine mode exceed 0.8 at all four wavelengths in the scenario I1, while the counterparts in the coarse mode approach 0.5 at 1020 nm and are less than 0.2 for the other three wavelengths. This is due to the weaker sensitivity of almucantar radiances to the coarse-mode m_r (as in Figure 4d) comparing to that for aerosol in the fine mode (as in Figure 3d). In general, adding the $DOLP_{alm}$, I_{PP}, or both the I_{PP} and $DOLP_{PP}$ in the inversion increases the DFS components for m_r of aerosols in both the fine and the coarse modes.

Table 4. Error for Retrieved Parameters Among A Priori, A Posteriori, and Glory Characterization[a]

	Error in Retrieved Parameters					
Entries	V (%)	r_{eff} (%)	v_{eff} (%)	m_r	m_i	Errors in Derived ω_A
A priori	100/100	80./80.	80./80.	0.150/0.150	0.0100/0.0050	0.151/0.198
Obs. I1	11./9.0	5.5/6.8	23./25.	0.015/0.065	0.0057/0.0038	0.037/0.085
Obs. I2	4.1/5.5	1.8/4.4	10./18.	0.008/0.037	0.0041/0.0032	0.024/0.073
Obs. P1	2.3/2.9	1.3/3.5	7.2/12.	0.005/0.035	0.0033/0.0030	0.019/0.068
Obs. P2	4.9/6.2	1.9/4.9	11./19.	0.009/0.040	0.0044/0.0034	0.026/0.076
Glory[b]	–	10	40	0.020	–	0.03

[a]Results of our work are averaged values for three aerosol types and for solar zenith angles from 40° to 75°.
[b]Referred to *Mishchenko et al.* [2004].

Particularly, DFS components achieve the most significant rise in the scenario P1 by climbing to 0.95–1.0 in the fine mode and to 0.4–0.8 in the coarse mode. Also shown in Figure 7a, an increasing pattern with solar zenith angles is found in the DFS components for the fine-mode aerosol at larger wavelengths because stronger sensitivity occurs in larger scattering angles.

As expected, the retrieval of m_r can be more accurate by adding additional measurements. According to Figures 7c and 7d, the a posteriori error in m_r averaged on the four spectral bands is ~ 0.015 (0.065) for aerosols in the fine (coarse) mode from measurements in the scenario I1. In contrast, it is reduced to 0.008 (0.037), 0.005 (0.035), and 0.009 (0.040) in the scenarios I2, P1, and P2, respectively. Retrieval errors in the coarse-mode m_r are larger in shorter spectral wavelengths because of weaker sensitivity to the I_{alm} and DOLP. For instance of the scenario P1, it is about 0.06 at 440 nm, 0.035 at 675 nm, and 0.02 at 870 and 1020 nm.

The DFS components for the m_i are shown in Figures 8a and 8b, and the corresponding retrieval errors in m_i are displayed in Figures 8c and 8d. Similar to those for the m_r, DFS components for retrieving the m_i are larger in the fine mode and show an increasing pattern with the solar zenith angle. Observations in the scenario P1 always yield largest DFS components and smallest retrieval error for the m_i, followed by the scenarios P2 and I2. Observations in the scenario I1 offer the m_i retrieval with largest error. If averaged on the solar zenith angles and aerosol types, the retrieval error in the m_i is 0.006 (0.004) for aerosol in the fine (coarse) mode in the scenario I1 and can be reduced to 0.003 (0.003) in the scenario P1.

4.2.3. Single-Scattering Albedo

Aerosol single-scattering albedo ω_A is an intermediate rather than a directly retrieved parameter. The error in ω_A can be estimated from $\hat{\mathbf{S}}$ with equation (4). The ω_A for each aerosol mode uniquely depends on the light wavelength and aerosol microphysical parameters including r_{eff}, v_{eff}, m_r, and m_i, although the m_i impacts ω_A most significantly [*Hansen and Travis*, 1974]. Required derivatives of ω_A to these parameters in the equation (4) can be obtained from the linearized Mie code integrated into the UNL-VRTM. We calculated uncertainties in the ω_A for each wavelength and each aerosol type, and the averaged values are summarized in Table 4. Observations in these four scenarios can retrieve ω_A with the uncertainty of 0.037, 0.024, 0.019, and 0.026 for the fine mode and 0.085, 0.073, 0.068, and 0.076 for the coarse mode, respectively. This agrees with the conclusion of *Hasekamp and Landgraf* [2005] that ω_A retrieval uncertainty can be reduced by adding polarization measurements, although only the fine-mode ω_A retrieval with polarization involved can meet the accuracy requirements (0.03) for accurate climate forcing estimates [*Mishchenko et al.*, 2004]. We noted that the mean uncertainty in the coarse-mode ω_A exceeds 0.06 in all of these four scenarios, but higher accuracy may be achieved under coarse-dominated conditions as shown in the following section. We also note that our result contradicts with findings in *Li et al.* [2009] who demonstrated that AERONET polarimetric measurements have no sensitivity to the imaginary part of the refractive index. This could pertain to the differences in assumptions of aerosol particle shape: sphere in this study while spheroid in *Li et al.* [2009]. *Dubovik et al.* [2006] also found weak sensitivity of polarization to the refractive index of nonspherical particles.

5. Sensitivity of Retrieval Error to AOD and fmf_V

The performance of retrieval usually varies with aerosol conditions like the aerosol loading and the prevalence of aerosol in either the fine or the coarse modes (e.g., fine-mode volume fraction, fmf_V). As a result, uncertainties in aerosol retrievals can depend much more strongly on the AOD than they do on the properties of an individual aerosol model [*Knobelspiesse et al.*, 2012]. For the same reason, the inversion of refractive indices and ω_A in the current AERONET algorithm is confined to the condition when the 440 nm AOD is larger than 0.4 [*Dubovik et al.*, 2000; *Holben et al.*, 2006]. Our analysis above, which focused on three aerosol types by a constant AOD value at 440 nm ($\tau_{440} = 1.0$), is insufficient to represent variable global conditions. At the same time, we also found noticeable variability of the DFS components and a posteriori errors existing among three aerosol types with different fmf_V, especially for the coarse-mode parameters. Thus, it is necessary to investigate how aerosol conditions affect the retrieval error, in order to answer the following questions: (1) Under what aerosol conditions are the AERONET measurements (with and without polarization) capable of yielding retrievals with sufficient accuracy? And (2) what aerosol conditions can allow the retrieval for both fine and coarse aerosol modes simultaneously (hereafter bimodal retrieval)?

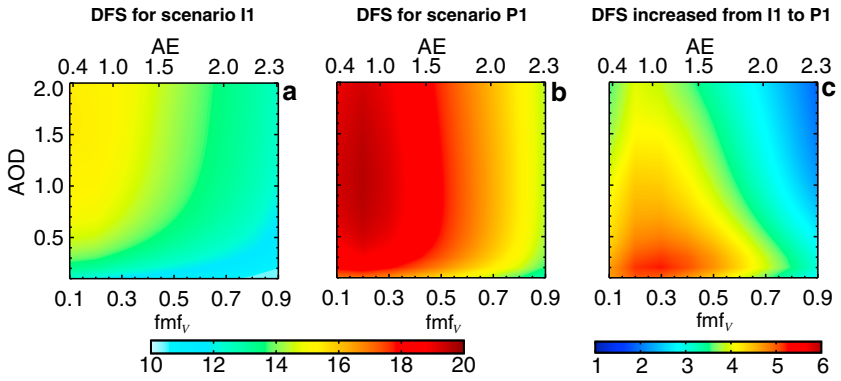

Figure 9. Contours of DFS as a function of fmf$_V$ and AOD in scenarios (a) I1 and (b) P1. (c) The difference of DFS between Figures 9a and 9b. Simulations are for solar zenith angle of 55°. The top abscissa denotes Ångström exponent (AE).

We expand our analysis for the τ_{440} ranging from 0.1 to 2.0 and for the fmf$_V$ from 0.1 to 0.9. In practice, the fmf$_V$ is inaccessible prior to inversion. Instead, we use the Ångström exponent (AE) from 870 to 1020 nm together with τ_{440} to define the aerosol conditions, because the AE in the longer paired wavelength is highly related to the fmf$_V$ [*Schuster et al.*, 2006; *Xu et al.*, 2015] and immediately available from the AERONET direct Sun measurements. With the aerosol properties defined in Table 2, the fmf$_V$ from 0.1 to 0.9 gives AE values from 0.35 to 2.3. We exclude the scenarios of I2 and P2 in our following analysis, because the scenario P1 demonstrates the most superior performance and is also the focus of our algorithm development [*Xu et al.*, 2015].

Figures 9a and 9b display the contours of DFS as a function of the AE (or fmf$_V$) and τ_{440} in the scenarios I1 and P1, respectively. We found that the DFS decreases with an increasing AE and fmf$_V$ for the same AOD. This is attributed to the fact that the coarse-mode parameters are more difficult to retrieve than their fine-mode counterparts, restrained by their weaker sensitivities to the I_{alm} and the DOLP$_{\mathrm{PP}}$. Thus, the decrease in the coarse-mode fraction significantly reduces the aerosol information for coarse-mode parameters but retains the information for fine-mode parameters, resulting in decreases in the total DFS. We also notice from Figure 9a that the DFS increases with an increasing AOD in the scenario I1. However, AOD change has less impact in the scenario P1 (Figure 9b). For example, the DFS values are lower than 14 when AOD < 0.4 in the scenario I1, whereas even larger DFS can be found in the scenario P1 when AOD < 0.2. Therefore, we may expect that the inversion in the scenario P1 will be capable to retrieve aerosol parameters in conditions of lower aerosol loading and may bring down the τ_{440} threshold of 0.4 from the current AERONET inversion algorithm to retrieve the refractive index and ω_{A}. Finally, as indicated in Figure 9c, the addition of I_{PP} and DOLP$_{\mathrm{PP}}$ in the inversion can add two to five pieces of useful information. Such improvement occurs in all aerosol conditions but is more dominated when enough coarse particles are present: fmf$_V < 0.5$ (or AE < 1.6), in which the radiance-only inversion usually yields a large retrieval error for the fine-mode aerosol. The contours of DFS components for each individual retrieved parameter can be found in Figure S2 in the supporting information.

In Figure 10, we show the contours of the a posteriori error $\hat{\epsilon}$ for each individual parameter in the scenarios I1 and P1, respectively. Overall, observations in the P1 scenario offer more accurate retrievals for all of these parameters in both the fine and the coarse aerosol modes. In both scenarios, the $\hat{\epsilon}$ decreases for fine-mode parameters and increases for coarse-mode parameters with increasing AE (or fmf$_V$) for the same τ_{440}, indicating that the relative contribution of fine and coarse modes determines the relative information of each mode. Extreme cases are fmf$_V$ of 1 or 0, i.e., the absence of the coarse- or fine-mode aerosols, which certainly will only allow a monomodal retrieval. Thus, the bimodal retrieval, especially for refractive indices, requires that aerosols reach certain mixture conditions to contain enough information for both modes. For example in the scenario I1, while the fine-mode r_{eff} can be well retrieved with 5% accuracy when the fmf$_V > 0.2$ at τ_{440} of 0.5 (Figure 10b), the fmf$_V > 0.3$ is required to ensure the $\hat{\epsilon} < 0.02$ in the fine-mode m_{r} (Figure 10d). Comparing to the change of the fmf$_V$, the change of τ_{440} has less impact on the $\hat{\epsilon}$ of the PSD parameters; this impact occurs in low aerosol loadings. For example, Figure 10f shows

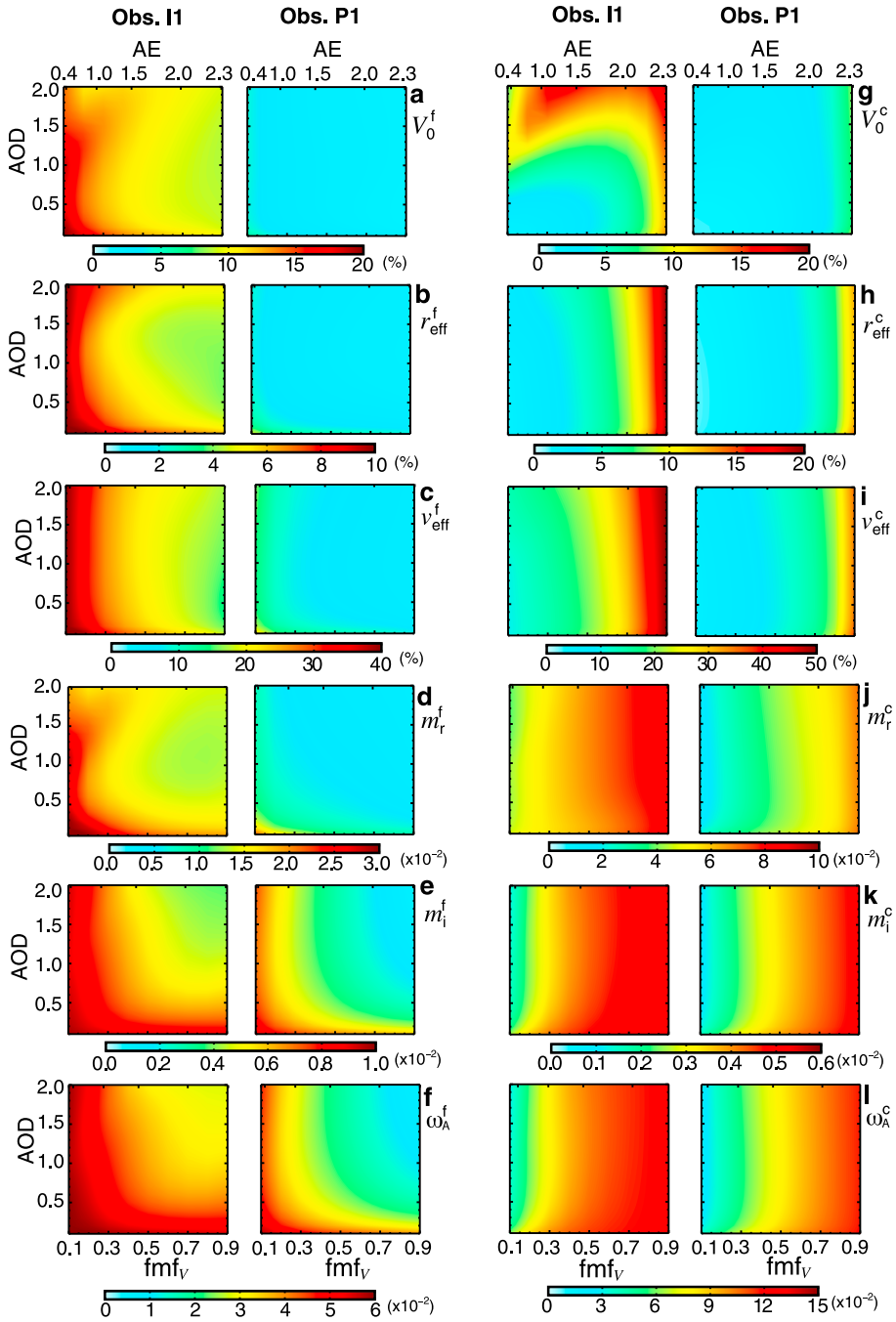

Figure 10. Retrieval uncertainties as a function of fmf$_V$ (or AE) and AOD for each individual aerosol parameters in both (a–f) the fine and (g–l) the coarse modes: V_0 (Figures 10a and 10g), r_{eff} (Figures 10b and 10h), v_{eff} (Figures 10c and 10i), m_r (Figures 10d and 10j), m_i (Figures 10e and 10k), and ω_A (Figures 10f and 10l). Two subpanels in each panel indicate observations in the scenarios I1 and P1, respectively. Simulations are for solar zenith angle of 55°. The *x* and *y* axes are identical to those in Figure 9. Relative uncertainties are shown for V_0, r_{eff}, and v_{eff}, while absolute errors are shown for m_r, m_i, and ω_A. Retrieval errors for m_r, m_i, and ω_A are averaged values over the four spectral bands.

that a minimum of ~ 0.4 for τ_{440} is required in the scenario I1 to guarantee a retrieval error in the fine-mode ω_A less than 0.04 when fmf$_V > 0.5$.

From Figure 10, we can identify required aerosol conditions in terms of the AE and τ_{440} in order to achieve the anticipated accuracy $\langle \in \rangle$, which are summarized in Table 5. Clearly, observations with polarization can

Table 5. Required Aerosol Conditions (τ_{440} and AE) to Achieve Anticipated Retrieval Accuracy $\langle \in \rangle$ for Observations in Scenarios I1 and P1[a]

Aerosol Parameters		$\langle \in \rangle$	Obs. Scenario I1		Obs. Scenario P1	
			τ_{440}	AE	τ_{440}	AE
V	Fine	10%	>0.3	>1.5	All	All
	Coarse	10%	<1.3	<2.2	All	All
r_{eff}	Fine	5%	>0.3	>1.3	All	All
	Coarse	10%	All	<2.0	All	<2.2
v_{eff}	Fine	20%	>0.3	>1.5	All	All
	Coarse	30%	All	<1.8	All	<2.2
m_r	Fine	0.02	>0.4	**>1.0**	All	All
	Coarse	0.04	All	**<1.0**	All	<1.8
ω_A	Fine	0.04	>0.6	**>1.5**	>0.2	>0.7
	Coarse	0.08	>0.2	**<1.1**	All	<1.6

[a]"All" indicates conditions $0.1 < \tau_{440} < 2.0$ and $0.35 < AE < 2.3$. Bold entries indicate conditions that cannot allow bimodal retrievals. AE is reported for wavelengths of 870 nm and 1020 nm.

enable retrievals of equivalent accuracy in a lower aerosol loading. For example, the retrieval accuracy of 10% for the V_0 and r_{eff} and 30% for the v_{eff} in the fine mode requires τ_{440} to be larger than 0.3 for inversion in the scenario I1 (Figures 10a–10c). In contrast, inversion in the scenario P1 can easily ensure retrievals of the same accuracy when τ_{440} is 0.1. For the fine-mode m_r retrieval, an accuracy of 0.04 requires $\tau_{440} > 0.4$ for the inversion I1 but $\tau_{440} > 0.2$ for the inversion P1 (Figure 10d). Moreover, the radiance-only inversion is unable to achieve bimodal retrievals of m_i and ω_A under any circumstance, because $AE > 1.5$ is necessary for retrieving the fine-mode ω_A (Figure 10f); meanwhile, $AE < 1.1$ is required for its coarse-mode retrieval (Figure 10l). This agrees with *Dubovik et al.* [2000] in that the retrieval of refractive indices for both fine and coarse mode is essentially nonunique due to limited information in the AERONET (radiance-only) observations. In contrast, observations in the scenario P1 can allow bimodal retrievals of the m_i and ω_A when $0.7 < AE > 1.6$ and $\tau_{440} > 0.2$ (Figures 10f and 10l). Therefore, our retrieval algorithm [*Xu et al.*, 2015] using observations of scenario P1 is designed to retrieve bimodal refractive indices when τ_{440} and AE reach these criteria. In aerosol conditions beyond the criteria, bimodal PSD along with a monomodal refractive index will be retrieved by assuming that the refractive index is independent of the aerosol mode.

6. Conclusion

In an effort to improve the AERONET inversion by including additional polarization measurements, this study examines the potential microphysical aerosol information contained in the AERONET photopolarimetric observations. We have focused our analysis on how the addition of polarization measurements impacts the retrieval accuracy for the aerosol particle size distribution (PSD), spectral refractive index, and single-scattering albedo ω_A. A numerical testbed has been constructed to generate the synthetic AERONET radiance and degree of linear polarization (DOLP) over 440, 675, 870, and 1020 nm. We considered four scenarios of observations that do or do not include the DOLP for the inversion, i.e., (I1) direct Sun AOD and almucantar sky radiances, (I2) observations in the scenario I1 with additional radiance measurements in the solar principal plane, (P1) observations in the scenario I2 plus polarization measurements in the solar principal plane, and (P2) observations in the scenario I1 plus almucantar polarization. Measurements in the scenario I1 are those used in current AERONET inversion algorithm and thus represent a control experiment. For each observation scenario, we also considered three types of spherical aerosol particles to represent general aerosol climatology. The Bayesian statistical approach then was applied to relate information contained in those synthetic data and retrieval errors in aerosol physical parameters to the instrumental as well as the a priori characteristics. Then the error-normalized Jacobian, degree of freedom for signal (DFS), and the a posteriori error in each individual retrieved parameter were presented as functions of solar zenith angle for these observation scenarios.

The results show a remarkable increase in information by adding additional polarization and/or radiances into the inversion. Overall, observations in the scenario P1 yield the highest DFS, which is larger than that

in the scenario I1 by 2–5 for all defined aerosol types. This can be understood as polarization measurements in the solar principal plane, in comparing with sky radiances in solar almucantar, have complementary sensitivities with respect to retrieved aerosol parameters. Also, measurements in the principal plane allow a wider range of scattering angles and supplies more information on aerosol backscattering. In scenario P2, adding polarization in the solar almucantar offers an increase of approximately two pieces of information with DFS values slightly below those in scenario I2. We also note that the DFS increases with increasing solar zenith angle for all cases, resulting from more information contained in observations of a wider range of scattering angle.

We also analyzed the DFS components and the a posteriori uncertainty for each individual retrieved parameter. As expected, the smallest retrieval errors were always found in the scenario P1: 2.3% (2.9%) for the volume concentration, 1.3% (3.5%) and 7.2% (12%) for the effective radius and effective variance, 0.005 (0.035) for the real part of refractive index, and 0.019 (0.068) for the single-scattering albedo in the fine (coarse) mode. These values represent an error reduction from the scenario I1 of 79% (57%), 76% (49%), 69% (52%), 66% (46%), and 49% (20%), respectively. Uncertainties in retrieved parameters averaged among these three aerosol types are summarized in Table 4 for each observation scenario. While agreeing with previous studies [*Chowdhary et al*., 2001; *Waquet et al*., 2009; *Mishchenko et al*., 2007; *Hasekamp and Landgraf*, 2005] in that polarimetric retrieval can significantly improve the retrieval accuracy over the radiance-only retrieval, the retrieval uncertainties for the P1 scenario in this theoretical study are smaller than those past results. This indicates that the accurate retrieval with AERONET photopolarimetric measurements can allow us to retrieve more aerosol properties with the accuracy needed for long-term monitoring of the direct an indirect aerosol forcing of climate and for validating aerosol retrievals from space polarimetric remote sensing.

Seeking to answer under what conditions the inversions can achieve a mode-resolved aerosol refractive index and ω_A, we further investigated how the AOD (τ_{440}) and fine/coarse modal domination (in terms of Ångström exponent, or AE) influence the retrieving accuracy from observations in the scenarios I1 and P1. We found that adding principal plane polarization measurements can increase the DFS by up to ~5 in cases dominated by coarse-mode particles (fmf < 0.5), in which the radiance-only inversion usually yields larger retrieval uncertainty for fine-mode aerosol. As a consequence, these photopolarimetric observations can enable accurate retrievals in a lower aerosol loading when the τ_{440} is 0.1, except for the fine-mode m_r retrieval that requires $\tau_{440} > 0.2$. The analysis also agrees with *Dubovik et al*. [2000] in that the radiance-only inversion is unable to resolve bimodal m_i and ω_A under any circumstance. However, observations in the scenario P1 can allow bimodal retrievals of m_i and ω_A when $0.7 < \text{AE} < 1.6$. Such criteria can guide us in the practical retrieval algorithm to determine whether a monomodal or bimodal retrieval of the aerosol refractive index and ω_A is possible. In aerosol conditions beyond the criteria, bimodal PSD along with the mode-independent refractive index will be retrieved.

Finally, it should be noted that in our analysis the aerosol particles in each mode are assumed to be polydisperse homogeneous spheres. Although the linearized T-matrix code has been implemented in the forward model (UNL-VRTM), the simulation of scattering properties for large nonspherical particles (for example, spheroids) is still subject to computational limitations. It has been shown by *Dubovik et al*. [2006] and *Deuzé et al*. [2001] that information content in the polarimetric retrieval of refractive index for the coarse mode, especially nonspherical particles, is limited. Therefore, the results of our analysis are only applicable to spherical aerosol particles; the information content and retrieval accuracy may be degraded for nonspherical coarse aerosol type. Our future efforts will implement nonspherical treatment in order to more realistically represent mineral dust aerosols.

Acknowledgments

This research is supported by a NASA Earth and Space Science Fellowship managed by Mingying Wei, as well as the NASA Radiation Sciences Program and the Glory Mission Program managed by Hal Maring. We acknowledge the computational support from the Holland Computing Center at the University of Nebraska. We are also very grateful to Brent Holben and Oleg Dubovik for their encouragements and in-depth comments to the early version of this manuscript. The data used in this study can be accessed upon request through email (jwang7@unl.edu) to the corresponding author.

References

Ångström, A. (1929), On the atmospheric transmission of Sun radiation and on dust in the air, *Geogr. Ann.*, *11*, 156–166.

Boesche, E., P. Stammes, T. Ruhtz, R. Preusker, and J. Fischer (2006), Effect of aerosol microphysical properties on polarization of skylight: Sensitivity study and measurements, *Appl. Opt.*, *45*(34), 8790–8805.

Boucher, O., et al. (2013), Clouds and aerosols, in *Climate Change 2013: The Physical Science Basis. Contribution of Working Group I to the Fifth Assessment Report of the Intergovernmental Panel on Climate Change*, edited by T. F. Stocker et al., Cambridge Univ. Press, Cambridge, U. K., and New York.

Cairns, B., B. E. Carlson, A. A. Lacis, and E. E. Russell (1997), An analysis of ground-based polarimetric sky radiance measurements, in *Polarization: Measurement, Analysis, and Remote Sensing*, vol. 3121, edited by R. A. Chipman and D. H. Goldstein, pp. 382–393, Proc. SPIE, San Diego, Calif.

Chowdhary, J., B. Cairns, M. Mishchenko, and L. Travis (2001), Retrieval of aerosol properties over the ocean using multispectral and multiangle Photopolarimetric measurements from the Research Scanning Polarimeter, *Geophys. Res. Lett.*, *28*(2), 243–246.

Curcio, J. (1961), Evaluation of atmospheric aerosol particle size distribution from scattering measurements in the visible and infrared, *J. Opt. Soc. Am.*, *51*(5), 548–551.

Dave, J. V. (1971), Determination of size distribution of spherical polydispersions using scattered radiation data, *Appl. Opt.*, *10*(9), 2035–2044.

Deuzé, J. L., et al. (2001), Remote sensing of aerosols over land surfaces from POLDER-ADEOS-1 polarized measurements, *J. Geophys. Res.*, *106*(D5), 4913–4926, doi:10.1029/2000JD900364.

Drury, E., D. J. Jacob, R. J. D. Spurr, J. Wang, Y. Shinozuka, B. E. Anderson, A. D. Clarke, J. Dibb, C. McNaughton, and R. Weber (2010), Synthesis of satellite (MODIS), aircraft (ICARTT), and surface (IMPROVE, EPA-AQS, AERONET) aerosol observations over eastern North America to improve MODIS aerosol retrievals and constrain surface aerosol concentrations and sources, *J. Geophys. Res.*, *115*, D14204, doi:10.1029/2009JD012629.

Dubovik, O. (2004), Optimization of numerical inversion in photopolarimetric remote sensing, in *Photopolarimetry in Remote Sensing*, edited by G. Videen, Y. Yatskiv, and M. Mishchenko, pp. 65–106, Springer, Netherlands.

Dubovik, O., and M. D. King (2000), A flexible inversion algorithm for retrieval of aerosol optical properties from Sun and sky radiance measurements, *J. Geophys. Res.*, *105*(D16), 20,673–20,696, doi:10.1029/2000JD900282.

Dubovik, O., A. Smirnov, B. N. Holben, M. D. King, Y. J. Kaufman, T. F. Eck, and I. Slutsker (2000), Accuracy assessments of aerosol optical properties retrieved from Aerosol Robotic Network (AERONET) Sun and sky radiance measurements, *J. Geophys. Res.*, *105*(D8), 9791–9806, doi:10.1029/2000JD900040.

Dubovik, O., B. N. Holben, T. Lapyonok, A. Sinyuk, M. I. Mishchenko, P. Yang, and I. Slutsker (2002), Non-spherical aerosol retrieval method employing light scattering by spheroids, *Geophys. Res. Lett.*, *29*(10, GL0141506), doi:10.1029/2001gl014506.

Dubovik, O., et al. (2006), Application of spheroid models to account for aerosol particle nonsphericity in remote sensing of desert dust, *J. Geophys. Res.*, *111*, D11208, doi:10.1029/2005JD006619.

Dubovik, O., M. Herman, A. Holdak, T. Lapyonok, D. Tanre, J. L. Deuze, F. Ducos, A. Sinyuk, and A. Lopatin (2011), Statistically optimized inversion algorithm for enhanced retrieval of aerosol properties from spectral multi-angle polarimetric satellite observations, *Atmos. Meas. Tech.*, *4*(5), 975–1018.

Emde, C., R. Buras, B. Mayer, and M. Blumthaler (2010), The impact of aerosols on polarized sky radiance: Model development, validation, and applications, *Atmos. Chem. Phys.*, *10*(2), 383–396.

Frankenberg, C., O. Hasekamp, C. O'Dell, S. Sanghavi, A. Butz, and J. Worden (2012), Aerosol information content analysis of multi-angle high spectral resolution measurements and its benefit for high accuracy greenhouse gas retrievals, *Atmos. Meas. Tech.*, *5*(7), 1809–1821.

Grassl, H. (1971), Determination of aerosol size distributions from spectral attenuation measurements, *Appl. Opt.*, *10*(11), 2534–2538.

Hansen, J. E., and L. D. Travis (1974), Light scattering in planetary atmospheres, *Space Sci. Rev.*, *16*, 572–610.

Hasekamp, O. P., and J. Landgraf (2005), Retrieval of aerosol properties over the ocean from multispectral single-viewing-angle measurements of intensity and polarization: Retrieval approach, information content, and sensitivity study, *J. Geophys. Res.*, *110*, D20207, doi:10.1029/2005JD006212.

Hasekamp, O. P., and J. Landgraf (2007), Retrieval of aerosol properties over land surfaces: Capabilities of multiple-viewing-angle intensity and polarization measurements, *Appl. Opt.*, *46*(16), 3332–3344.

Haywood, J., and O. Boucher (2000), Estimates of the direct and indirect radiative forcing due to tropospheric aerosols: A review, *Rev. Geophys.*, *38*(4), 513–543, doi:10.1029/1999RG000078.

Herman, B. M., S. R. Browning, and J. A. Reagan (1971), Determination of aerosol size distributions from lidar measurements, *J. Atmos. Sci.*, *28*(5), 763–771.

Hess, M., P. Koepke, and I. Schult (1998), Optical properties of aerosols and clouds: The software package OPAC, *Bull. Am. Meteorol. Soc.*, *79*(5), 831–844.

Holben, B. N., T. F. Eck, I. Slutsker, D. Tanre, J. P. Buis, A. Setzer, E. Vermote, J. A. Reagan, and Y. J. Kaufman (1994), Multi-band automatic Sun and sky scanning radiometer for measurement of aerosols, *Proc. Int. Symp. Phys. Meas. Signatures Remote Sens.*, *6*, 75–83.

Holben, B. N., et al. (1998), AERONET—A federated instrument network and data archive for aerosol characterization, *Remote Sens. Environ.*, *66*(1), 1–16.

Holben, B. N., T. F. Eck, I. Slutsker, A. Smirnov, A. Sinyuk, J. Schafer, D. Giles, and O. Dubovik (2006), Aeronet's version 2.0 quality assurance criteria, in *Remote Sensing of the Atmosphere and Clouds*, vol *6408*, edited by S.-C. Tsay, et al., 64080Q, Proc. SPIE, Goa, India, doi:10.1117/12.706524.

Kaufman, Y. J., A. Gitelson, A. Karnieli, E. Ganor, R. S. Fraser, T. Nakajima, S. Mattoo, and B. N. Holben (1994), Size distribution and scattering phase function of aerosol particles retrieved from sky brightness measurements, *J. Geophys. Res.*, *99*, 10,341–10,356, doi:10.1029/94JD00229.

Kaufman, Y. J., D. Tanre, and O. Boucher (2002), A satellite view of aerosols in the climate system, *Nature*, *419*, 215–223.

King, M. D., D. M. Byrne, B. M. Herman, and J. A. Reagan (1978), Aerosol size distributions obtained by inversions of spectral optical depth measurements, *J. Atmos. Sci.*, *35*(11), 2153–2167.

Knobelspiesse, K., B. Cairns, M. Mishchenko, J. Chowdhary, K. Tsigaridis, B. van Diedenhoven, W. Martin, M. Ottaviani, and M. Alexandrov (2012), Analysis of fine-mode aerosol retrieval capabilities by different passive remote sensing instrument designs, *Opt. Express*, *20*(19), 21,457–21,484.

Li, Z., L. Blarel, T. Podvin, P. Goloub, J.-P. Buis, and J.-P. Morel (2008), Transferring the calibration of direct solar irradiance to diffuse-sky radiance measurements for CIMEL Sun-sky radiometers, *Appl. Opt.*, *47*(10), 1368–1377.

Li, Z., et al. (2009), Improvements for ground-based remote sensing of atmospheric aerosol properties by additional polarimetric measurements, *J. Quant. Spectros. Radiat. Transfer*, *110*(17), 1954–1961.

Li, Z., L. Blarel, T. Podvin, P. Goloub, and L. Chen (2010), Calibration of the degree of linear polarization measurement of polarized radiometer using solar light, *Appl. Opt.*, *49*(8), 1249–1256.

Lucht, W., C. B. Schaaf, and A. H. Strahler (2000), An algorithm for the retrieval of albedo from space using semiempirical BRDF models, *IEEE Trans. Geosci. Remote Sens.*, *38*(2), 977–998.

Maignan, F., F.-M. Bréon, E. Fédèle, and M. Bouvier (2009), Polarized reflectances of natural surfaces: Spaceborne measurements and analytical modeling, *Remote Sens. Environ.*, *113*(12), 2642–2650.

Meland, B. S., X. Xu, D. K. Henze, and J. Wang (2013), Assessing remote polarimetric measurement sensitivities to aerosol emissions using the geos-chem adjoint model, *Atmos. Meas. Tech.*, *6*(12), 3441–3457.

Mishchenko, M. I., and L. D. Travis (1997), Satellite retrieval of aerosol properties over the ocean using polarization as well as intensity of reflected sunlight, *J. Geophys. Res.*, *102*(D14), 16,989–17,013, doi:10.1029/96JD02425.

Mishchenko, M. I., B. Cairns, J. E. Hansen, L. D. Travis, R. Burg, Y. J. Kaufman, J. Vanderlei Martins, and E. P. Shettle (2004), Monitoring of aerosol forcing of climate from space: Analysis of measurement requirements, *J. Quant. Spectros. Radiat. Transfer*, *88*(1–3), 149–161.

Mishchenko, M. I., B. Cairns, J. E. Hansen, L. D. Travis, G. Kopp, C. F. Schueler, B. A. Fafaul, R. J. Hooker, H. B. Maring, and T. Itchkawich (2007), Accurate monitoring of terrestrial aerosols and total solar irradiance: Introducing the Glory Mission, *Bull. Am. Meteorol. Soc.*, *88*(5), 677–691.

Myhre, G., et al. (2013), Anthropogenic and natural radiative forcing, in *Climate Change 2013: The Physical Science Basis. Contribution of Working Group I to the Fifth Assessment Report of the Intergovernmental Panel on Climate Change*, edited by T. F. Stocker et al., Cambridge Univ. Press, Cambridge, U. K., and N. Y.

Nadal, F., and F. M. Breon (1999), Parameterization of surface polarized reflectance derived from POLDER spaceborne measurements, *IEEE Trans. Geosci. Remote Sens.*, *37*(3), 1709–1718.

Nakajima, T., M. Tanaka, and T. Yamauchi (1983), Retrieval of the optical properties of aerosols from aureole and extinction data, *Appl. Opt.*, *22*(19), 2951–2959.

Nakajima, T., G. Tonna, R. Rao, P. Boi, Y. Kaufman, and B. Holben (1996), Use of sky brightness measurements from ground for remote sensing of particulate polydispersions, *Appl. Opt.*, *35*(15), 2672–2686.

Patterson, E. M., D. A. Gillette, and B. H. Stockton (1977), Complex index of refraction between 300 and 700 nm for Saharan aerosols, *J. Geophys. Res.*, *82*, 3153–3160, doi:10.1029/JC082i021p03153.

Phillips, D. L. (1962), A technique for the numerical solution of certain integral equations of the first kind, *J. ACM*, *9*(1), 84–97.

Ramanathan, V., P. J. Crutzen, J. T. Kiehl, and D. Rosenfeld (2001), Aerosols, climate, and the hydrological cycle, *Science*, *294*, 2119–2124.

Reid, J. S., et al. (2008), An overview of UAE^2 flight operations: Observations of summertime atmospheric thermodynamic and aerosol profiles of the southern Arabian Gulf, *J. Geophys. Res.*, *113*, D14213, doi:10.1029/2007JD009435.

Rodgers, C. D. (1998), Information content and optimisation of high spectral resolution remote measurements, *Adv. Space Res.*, *21*(3), 361–367.

Rodgers, C. D. (2000), *Inverse methods for atmospheric sounding: Theory and practice*, World Scientific, Singapore.

Sanghavi, S., J. V. Martonchik, J. Landgraf, and U. Platt (2012), Retrieval of aerosol optical depth and vertical distribution using O2 A- and B-band SCIAMACHY observations over Kanpur: A case study, *Atmos. Meas. Tech.*, *5*(5), 1099–1119.

Schuster, G. L., O. Dubovik, and B. N. Holben (2006), Angstrom exponent and bimodal aerosol size distributions, *J. Geophys. Res.*, *111*, D07207, doi:10.1029/2005JD006328.

Shannon, C. E. (1948), *The Mathematical Theory of Communication, Bell System Technical Journal*, vol. 27, pp. 379–423, Univ. of Illinoi Press, Urbana.

Shaw, G. E. (1979), Inversion of optical scattering and spectral extinction measurements to recover aerosol size spectra, *Appl. Opt.*, *18*(7), 988–993.

Smirnov, A., B. N. Holben, T. F. Eck, O. Dubovik, and I. Slutsker (2000), Cloud screening and quality control algorithms for the AERONET database, *Remote Sens. Environ.*, *73*, 337–349.

Spurr, R. (2008), LIDORT and VLIDORT: Linearized pseudo-spherical scalar and vector discrete ordinate radiative transfer models for use in remote sensing retrieval problems, in *Light Scattering Reviews 3*, edited by A. Kokhanovsky, pp. 229–275, Springer, Berlin.

Tanaka, M., T. Nakajima, and T. Takamura (1982), Simultaneous determination of the complex refractive index and size distribution of airborne and water suspended particles from light scattering measurements, *J. Meteorol. Soc. Jpn.*, *60*, 1259–1272.

Tanaka, M., T. Takamura, and T. Nakajima (1983), Refractive index and size distribution of aerosols as estimated from light scattering measurements, *J. Climate Appl. Meteorol.*, *22*(7), 1253–1261.

Twomey, S. (1963), On the numerical solution of Fredholm integral equations of the first kind by the inversion of the linear system produced by quadrature, *J. ACM*, *10*(1), 97–101.

Twomey, S., and H. B. Howell (1967), Some aspects of the optical estimation of microstructure in fog and cloud, *Appl. Opt.*, *6*(12), 2125–2131.

van de Hulst, H. C. (1981), *Light scattering by small particles*, Dover ed., Dover Publications, Mineola, New York.

Vermeulen, A., C. Devaux, and M. Herman (2000), Retrieval of the scattering and microphysical properties of aerosols from ground-based optical measurements including polarization: I. Method, *Appl. Opt.*, *39*(33), 6207–6220.

Wagner, R., T. Ajtai, K. Kandler, K. Lieke, C. Linke, T. Müller, M. Schnaiter, and M. Vragel (2012), Complex refractive indices of Saharan dust samples at visible and near UV wavelengths: A laboratory study, *Atmos. Chem. Phys.*, *12*(5), 2491–2512.

Wang, J., X. Xu, S. Ding, J. Zeng, R. Spurr, X. Liu, K. Chance, and M. Mishchenko (2014), A numerical testbed for remote sensing of aerosols, and its demonstration for evaluating retrieval synergy from a geostationary satellite constellation of GEO-CAPE and GOES-R, *J. Quant. Spectros. Radiat. Transfer*, *146*, 510–528.

Wanner, W., X. Li, and A. H. Strahler (1995), On the derivation of kernels for kernel-driven models of bidirectional reflectance, *J. Geophys. Res.*, *100*(D10), 21,077–21,089, doi:10.1029/95JD02371.

Waquet, F., B. Cairns, K. Knobelspiesse, J. Chowdhary, L. D. Travis, B. Schmid, and M. I. Mishchenko (2009), Polarimetric remote sensing of aerosols over land, *J. Geophys. Res.*, *114*, D01206, doi:10.1029/2008JD010619.

Wendisch, M., and W. Von Hoyningen-Huene (1994), Possibility of refractive index determination of atmospheric aerosol particles by ground-based solar extinction and scattering measurements, *Atmos. Environ.*, *28*(5), 785–792.

Xu, X., et al. (2015), Retrieval of aerosol microphysical properties from AERONET photopolarimetric measurements: 2. A new research algorithm and case demonstration, *J. Geophys. Res. Atmos.*, *120*, doi:10.1002/2015JD023113.

Yamamoto, G., and M. Tanaka (1969), Determination of aerosol size distribution from spectral attenuation measurements, *Appl. Opt.*, *8*(2), 447–453.

Yamasoe, M. A., Y. J. Kaufman, O. Dubovik, L. A. Remer, B. N. Holben, and P. Artaxo (1998), Retrieval of the real part of the refractive index of smoke particles from Sun/sky measurements during SCAR-B, *J. Geophys. Res.*, *103*(D24), 31,893–31,902, doi:10.1029/98JD01211.

Zeng, J., Q. Han, and J. Wang (2008), High-spectral resolution simulation of polarization of skylight: Sensitivity to aerosol vertical profile, *Geophys. Res. Lett.*, *35*, L20801, doi:10.1029/2008GL035645.